Journal Pre-proof

3D multifunctional porous pine carbon aerogels coupled with highly dispersed CoFe nanoparticles for robust electromagnetic wave response

Xiaojun Zeng , Xiawen Peng , Ya Ning , Xiao Jiang , Ronghai Yu , Xiaofeng Zhang

Please cite this article as: Xiaojun Zeng , Xiawen Peng , Ya Ning , Xiao Jiang , Ronghai Yu , Xiaofeng Zhang , 3D multifunctional porous pine carbon aerogels coupled with highly dispersed CoFe nanoparticles for robust electromagnetic wave response, *Journal of Materials Science & Technology* (2024), doi: https://doi.org/10.1016/j.jmst.2023.12.046

This is a PDF file of an article that has undergone enhancements after acceptance, such as the addition of a cover page and metadata, and formatting for readability, but it is not yet the definitive version of record. This version will undergo additional copyediting, typesetting and review before it is published in its final form, but we are providing this version to give early visibility of the article. Please note that, during the production process, errors may be discovered which could affect the content, and all legal disclaimers that apply to the journal pertain.

Highlights:

- 3D porous CWA-CoFe-NC aerogel with honeycomb-like structure is fabricated.
- CWA-CoFe-NC aerogel delivers outstanding EMW absorption performance.
- Good mechanical and thermal stability properties are realized in aerogel.

Research Article

3D multifunctional porous pine carbon aerogels coupled with highly dispersed CoFe nanoparticles for robust electromagnetic wave response

Xiaojun Zeng,[a,#,*] Xiawen Peng,[a,#] Ya Ning,[a] Xiao Jiang,[a] Ronghai Yu,[b] Xiaofeng Zhang[c,*]

[a] School of Materials Science and Engineering, Jingdezhen Ceramic University, Jingdezhen 333403, China

[b] School of Materials Science and Engineering, Beihang University, Beijing 100191, China

[c] Guangdong Academy of Science, Guangdong Institute of New Materials, National Engineering Laboratory for Modern Materials Surface Engineering Technology, The Key Lab of Guangdong for Modern Surface Engineering Technology, Guangzhou 510650, China

* Corresponding authors.

E-mail addresses: zengxiaojun@jcu.edu.cn (X.J. Zeng), zxf200808@126.com (X.F. Zhang).

[#] These authors contributed equally to this work.

Abstract

Functional carbonaceous materials with controllable morphology, low apparent density, large surface area, and high porosity starting from natural precursors using environmentally friendly processes are an appealing topic in the electromagnetic wave (EMW) field. In this work, renewable pine woods with ordered pore channels are selected to load highly dispersed CoFe alloy nanoparticles formed by in-situ pyrolysis reaction between Fe_3O_4 nanospheres and ZIF-67 nanoparticles. The constructed three-dimensional (3D) porous CWA-CoFe-NC aerogel inherits the characteristics of highly dispersed small CoFe alloy nanoparticles, porous carbon aerogel with rectangular honeycomb-like structure, and abundant N heteroatoms. Therefore, CWA-CoFe-NC aerogel achieves an excellent EMW absorption performance with reflection loss (R_L) values of -61.6 and -58.2 dB at matching thicknesses of 3.7 and 1.2 mm, respectively. Benefiting from the reasonable design of the composite structure and composition, 3D porous aerogel also enables great potential for multifunctional applications. Particularly, good lightweight and mechanical properties are realized in the CWA-CoFe-NC aerogels due to their ordered pore channels and abundant rectangular pores. Furthermore, good flame retardant performance can ensure the serviceability of the target device in high/low-temperature environments. In addition, CWA-CoFe-NC aerogels show good thermal stability and thermal management characteristics. This work provides a novel and effective method for the preparation of lightweight, high-performance, and multifunctional EMW absorbers.

Keywords: Pine carbon aerogel, EMW absorption, lightweight, mechanical, flame

retardant, thermal stability

1. Introduction

With the rapid development of electronic devices and communication technologies represented by emerging 5G wireless systems and wearable portable devices, the threat of electromagnetic radiation pollution to human health and the environment is becoming increasingly serious. This type of harm is mainly reflected in electromagnetic interference between electronic components, electromagnetic information leakage, and human nerve damage [1,2]. Electromagnetic pollution has become an inevitable social problem [3-8], so exploring high-performance electromagnetic wave (EMW) absorption materials is of great significance. Among them, lightweight, thin matching thickness (d ⩽ 1.5 mm), strong reflection loss (R_L ⩽ -50 dB), wide effective absorption bandwidth (EAB, R_L < -10 dB), and multifunctional EMW absorption materials have received wide attention [9,10].

The existing EMW absorbers can be mainly divided into dielectric, magneto-dielectric, and resistive absorbers, among which resistive absorbers have attracted much attention due to the high conversion of electromagnetic energy to thermal energy [11,12]. Typical resistive EMW absorbers are conductive polymers and carbon materials, such as traditional graphite [13], carbon fibers [14], carbon nanotubes [15], and graphene oxide [16]. Carbon materials generally have low resistivity and cannot effectively "retain" electromagnetic waves, so the carbon materials for EMW absorption often require special treatment. Notably, porous carbon is receiving more

and more attention due to its good electrical conductivity, large specific surface area, controllable pore size, and low density [17]. Specifically, porous materials can be considered as a mixture of solid and air, and are effective media. The presence of porous structures can reduce the dielectric constant and improve the impedance matching, allowing more EMW to enter, which can further increase the scattering and reflection of EMW as well as the propagation path of EMW [18]. Furthermore, the rich porous structure provides more opportunities for loading highly dispersed absorption sites within the pores [19]. The synergistic effect between magnetic loss induced by metal alloys and dielectric loss of porous carbon can effectively improve the EMW absorption performance [20]. However, many porous carbon EMW absorbers are synthesized from fossil resources [21], which can seriously pollute the environment and cannot be used as a material object for sustainable development. Besides, many porous carbon absorbers are based on synthetic matrix implanted with particles that facilitate EMW absorption to achieve good performance [22]. These EMW absorption materials are not only complex and expensive to synthesize, but also their structures are affected by many factors, which makes it difficult to high-performance EMW absorption materials with multifunctional performance. The increasing demand for military security and healthy living has led to more applications of EMW absorption materials in high-tech fields [23]. Therefore, it is feasible to develop highly effective porous carbon-based EMW absorbers with versatility to meet complex application scenarios.

As a countermeasure, biomass materials have received increasing attention due to

their abundant resources and environmental friendliness [24,25]. The multi-level structure of the biomass material is very helpful for EMW absorption and provides a stable broad substrate for absorption sites. Moreover, the feedstock comes from nature and has a low environmental impact. Previous work shows that many biomass materials can be used to prepare porous carbon materials as EMW absorbers, such as bacterial cellulose [26], walnut shell [27], rice husk [28], cigarette filters [29], and eggshells [30]. Biomass materials can be directly converted into porous carbon materials through a simple carbonization process. However, when using these biomasses as templates, although the structure is stable, the integrated structure is problematic and the final compositions lack multifunctional properties. Inspired by the unique anisotropic porous structure of abundant virgin wood [31], some researchers have proposed the development of multifunctional EMW absorbers using virgin wood as a matrix. The virgin wood is a renewable resource, harmless to the environment, and widely distributed. Furthermore, virgin wood exhibits low curvature, unique arrangement structure, high porosity, and high specific surface area. Its three-dimensional (3D) network structure can greatly reduce the density of the material, making the absorber lightweight. In addition, virgin wood has anisotropic thermal conductivity and good mechanical properties, providing more possibilities for developing multifunctional properties. However, single-component carbon materials have high electrical conductivity, which will lead to impedance mismatch and affect EMW absorption capacity [32,33]. Therefore, high-performance EMW absorbers can be realized by combining materials with complementary properties and carbon-based

6

materials into composites [34].

Herein, 3D porous carbon aerogel derived from pine wood is used as a template to load highly dispersed CoFe alloy nanoparticles, which are derived from the reaction of ZIF-67 and Fe_3O_4 nanospheres, in combination with the hydrothermal method and heat treatment process. The uniform linear channel structure of the pine carbon aerogel leads to multiple scattering, reflection, and absorption of EMW. Furthermore, the ZIF-67-derived graphitic carbon and the pine carbon aerogel build into a conductive network to enhance the conductive loss. At the same time, numerous interfaces are constructed in CWA-CoFe-NC aerogel, leading to good interface polarization. The formed CoFe alloy nanoparticles show high magnetic losses. Therefore, the synergistic effect of good dielectric loss, magnetic loss, and impedance matching promotes the EMW absorption performance, with R_L values of -61.6 and -58.2 dB at matching thicknesses of 3.7 and 1.2 mm, respectively. Thanks to the reasonable design of the composite structure and composition, 3D porous aerogel also shows great potential for multifunctional applications such as good lightweight, mechanical, flame retardant, and thermal stability performance.

2. Experimental

2.1 Materials

Sodium sulfite (Na_2SO_3, >97.0%), sodium hydroxide (NaOH, >96.0%), hydrogen peroxide (H_2O_2, >30.0%), sodium dodecyl benzene sulfonate (SDBS, >83.0%), ferric chloride hexahydrate ($FeCl_3 \cdot 6H_2O$, >99.0%), sodium acetate (CH_3COONa, >99.0%),

7

polyethylene pyrrolidone K30 (PVP K30, GR), cobalt nitrate hexahydrate (Co(NO$_3$)$_2$·6H$_2$O, >98.5%), 2-methylimidazole (2-MIM, >98.0%), methanol (>99.5%), and ethylene glycol (EG, >96.0%) were purchased from Sinopharm Chemical Reagent Corporation Limited. All reagents were used directly without further purification.

2.2 Preparation of iron oxide (Fe$_3$O$_4$) nanospheres

Fe$_3$O$_4$ nanospheres were prepared by a solvothermal method. Briefly, 0.33 g of SDBS was added to 32 mL of EG and magnetically stirred at room temperature to form a uniform solution. Then, FeCl$_3$·6H$_2$O (1.08 g) and CH$_3$COONa (1.97 g) were added to the solution and stirred for 30 min. The uniform solution was transferred into a 50 mL PTFE-lined stainless steel autoclave and kept in the oven at 180 ℃ for 8 h. The obtained powder was centrifuged, washed with deionized water and ethanol, and vacuum dried at 70 ℃ for 12 h to obtain Fe$_3$O$_4$ nanospheres.

2.3 Preparation of delignified wood aerogel (WA)

Delignified wood aerogel (WA) was prepared by a freeze-dry strategy. Specifically, the pine wood (10 mm × 10 mm × 10 mm) was boiled and stirred at 85 ℃ in a mixed solution of NaOH (2.5 mol/L) and Na$_2$SO$_3$ (0.4 mol/L) for 8 h, and then transferred to the boiled deionized water for multiple times to remove the residual lignin. The treated pine wood was then stirred in a H$_2$O$_2$ solution (2.45 mol/L) at 80 ℃ for 3 h. The obtained pine wood was freeze-dried at -96 ℃ for 24 h to achieve the WA.

2.4 Preparation of CWA-CoFe-NC

Typically, Co(NO$_3$)$_2$·6H$_2$O (0.804 g), PVP K30 (0.3 g), and Fe$_3$O$_4$ nanospheres

(0.15 g) were dispersed in 20 mL of deionized water, and then WA was impregnated and extruded in the mixed solution for several times. Afterward, 2-MIM (2.624 g) was dispersed in 40 mL of methanol solution, and then the above-treated WA was soaked in the solution and left for 12 h at room temperature. The WA was moved out and washed several times with ethanol to obtain a WA-ZIF-Fe_3O_4 sample. Finally, the sample was placed in a tuber furnace and heated to 800 °C at the rate of 1.5 °C min^{-1} in an argon atmosphere and held for 2 h to obtain the target CWA-CoFe-NC sample. To investigate the effect of pyrolysis temperature on the EMW absorption performance, the pyrolysis temperature was optimized to 700, 800, and 900 °C, respectively. In addition, CWA-Co-NC (without adding Fe_3O_4), CWA-Fe (without adding Co^{2+} and 2-MIM), and pure CWA were prepared with similar conditions for comparison.

2.5 Material characterization

The microstructures and crystal phases of the as-fabricated samples were analyzed by utilizing field-emission scanning electron microscopy (FE-SEM, HITACHI SU8010), transmission electron microscopy (TEM, FEI Talos F200S), and X-ray diffraction (XRD) spectrometry (D8 Advance, Bruker, Germany) with a Cu K_α radiation source (λ = 0.15406 nm, 40 kV, 30 mA). X-ray photoelectron spectroscopy (XPS, Thermo escalade 250Xi) was conducted on a Thermo escalade 250Xi to observe the chemical state of the as-made samples.

2.6 Electromagnetic performance evaluation

Agilent E5071C vector network analyzer was used to measure the electromagnetic

parameters of the sample in the microwave frequency range (2-18 GHz) to evaluate its EMW absorption performance. The mixture of sample and paraffin (mass ratio of 4:6) was pressed into a test ring with an inner diameter of 3.04 mm, an outer diameter of 7.00 mm, and a thickness of approximately 2.50 mm. According to the complex permittivity ($\varepsilon_r = \varepsilon' - j\varepsilon''$) and the complex permeability ($\mu_r = \mu' - j\mu''$), the reflection loss (R_L) of the sample can be calculated by the following equation [35]:

$$R_L = 20\log_{10}|(Z_{in} - Z_0)/(Z_{in} + Z_0)| \tag{1}$$

$$Z_{in} = Z_0(\mu_r/\varepsilon_r)^{1/2}\tanh[j(2\pi fd/c)(\mu_r\varepsilon_r)^{1/2}] \tag{2}$$

where the Z_0 and Z_{in} represent the free-space impedance and input impedance, respectively. d, f, and c denote thickness, frequency, and light velocity, respectively.

3. Results and discussion

Fig. 1 depicts the preparation process of 3D porous CWA-CoFe-NC. As shown in Fig. 1, environmentally friendly, economical, and renewable 3D porous pine wood was chosen as the carbon framework. After removing lignin and cellulose, a light delignified wood aerogel (WA) was obtained, which inherits the high porosity and special arrangement structure of the natural wood matrix. Subsequently, 3D porous WA was immersed in a solution containing PVP, Co^{2+}, Fe_3O_4, as well as 2-MIM solution, to embed the Fe_3O_4 nanosphere and resulting ZIF-67 into the WA channel wall. Finally, during the pyrolysis process, Co ions in ZIF-67 react with Fe_3O_4 to form CoFe nanoparticles, which are encapsulated by nitrogen-doped carbon (NC) in situ and tightly embedded on the channel surface of CWA.
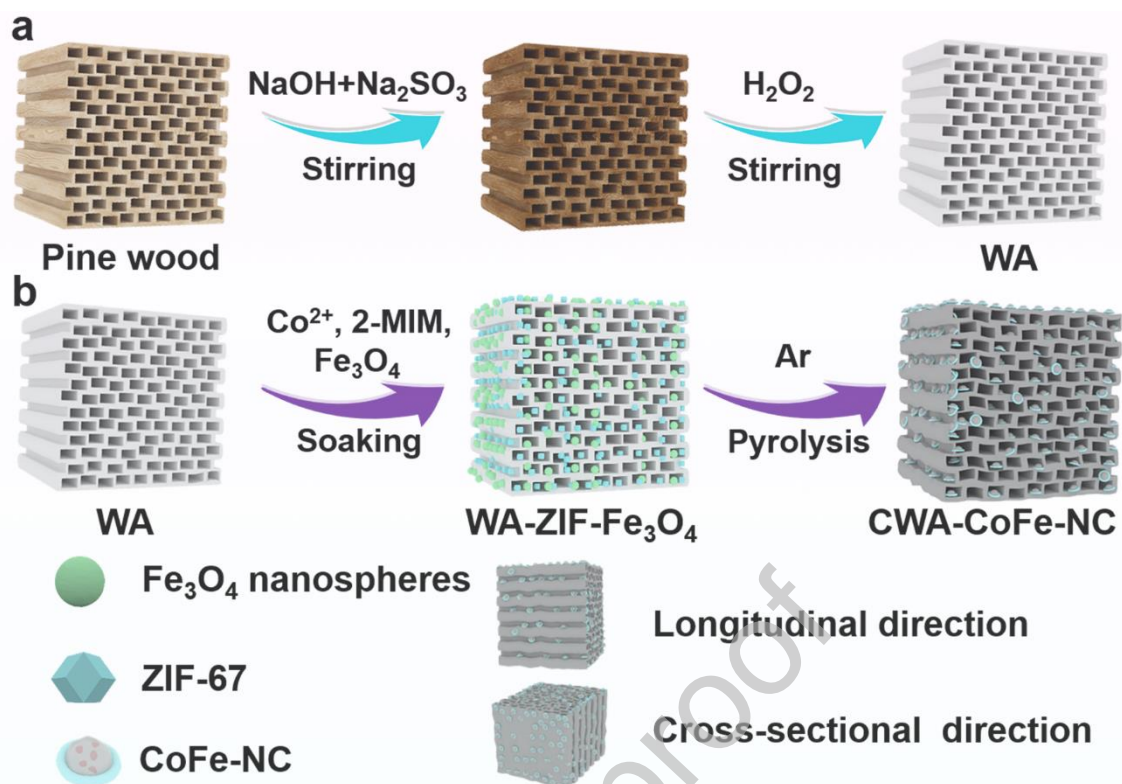
10

Fig. 1. Scheme showing the fabrication process of 3D porous CWA-CoFe-NC.

The crystal structures of the samples were characterized by X-ray diffraction (XRD) spectrometry. As shown in Fig. 2(a), pure pine has two broad peaks at 23.8° and 44° after calcination, corresponding to the (200) and (101) crystal planes of graphite, which are also typical amorphous carbon peaks. This is consistent with the results of other biomass carbonaceous materials heated at high temperatures [36]. The CWA-Co-NC obtained by loading ZIF-67 and calcination has two typical Co phases (PDF#15-8063) diffraction peaks at 44.1° and 51.5°, while the CWA-Fe obtained by loading Fe_3O_4 and calcination has typical diffraction peaks of Fe phase (PDF#06-0696). This indicated that ZIF-67 and Fe_3O_4 are well transformed into metal species after carbonization at high temperatures. For CWA-CoFe-NC, typical Co_3Fe_7 alloy peaks are found at 44.75° and 65.1°, indicating that during heat treatment, ZIF-67 and Fe_3O_4 react to form the alloy [37], which contributes to the enhancement of the EMW

11

absorption capacity.

The chemical composition of CWA-CoFe-NC and CWA-Co-NC was further characterized by X-ray photoelectron spectroscopy (XPS). XPS spectra in Figs. S1 and S2 in Supplementary Information show the presence of Co, C, N, and O elements in both CWA-Co-NC and CWA-CoFe-NC, except for the presence of Fe element in CWA-CoFe-NC. From Fig. 2(b), the Fe 2p spectra for CWA-CoFe-NC can be resolved into two peaks at 712.45 and 723.84 eV, which can be assigned to Fe $2p_{3/2}$ and Fe $2p_{1/2}$, respectively [38]. In the high-resolution Co 2p spectra, for CWA-CoFe-NC, the peaks at 781.47 and 797.53 eV are hailed as the characteristic Co $2p_{3/2}$ and Co $2p_{1/2}$ spin tracks. Furthermore, two equivalent satellite peaks appear at 786.02 and 803.7 eV (Fig. 2(c)) [39]. The Co 2p spectra for CWA-Co-NC show similar peaks. On the other hand, the high-resolution C 1s spectra of CWA-CoFe-NC consist of two carbon peaks (C-C (284.8 eV) and C-N (285.9 eV)), while the C 1s spectra of CWA-Co-NC consist of three carbon peaks of C-C (284.8 eV), C-N (285.9 eV), and C=O (288.8 eV) (Fig. 2(d)) [40]. This result indicates that the carbon is doped by N heteroatoms, which originates from the pyrolysis of ZIF-67. The high-resolution N 1s spectra of CWA-CoFe-NC and CWA-Co-NC are presented in Fig. 2(e). The fitted peak at 401 eV is ascribed to the signal of δ^+ (N) (e.g., NH_4^+ = 401 eV), as expected for the δ^+ (N) peak in pine after calcination [41]. The abundant N heteroatoms in the CWA matrix contribute to the dipolar polarization and EMW absorption capability. In addition, the O 1s spectra of CWA-CoFe-NC and CWA-Co-NC can be deconvoluted into three peaks centered at 532.04, 533.15, and 536 eV (Fig. 2(f)), corresponding to -

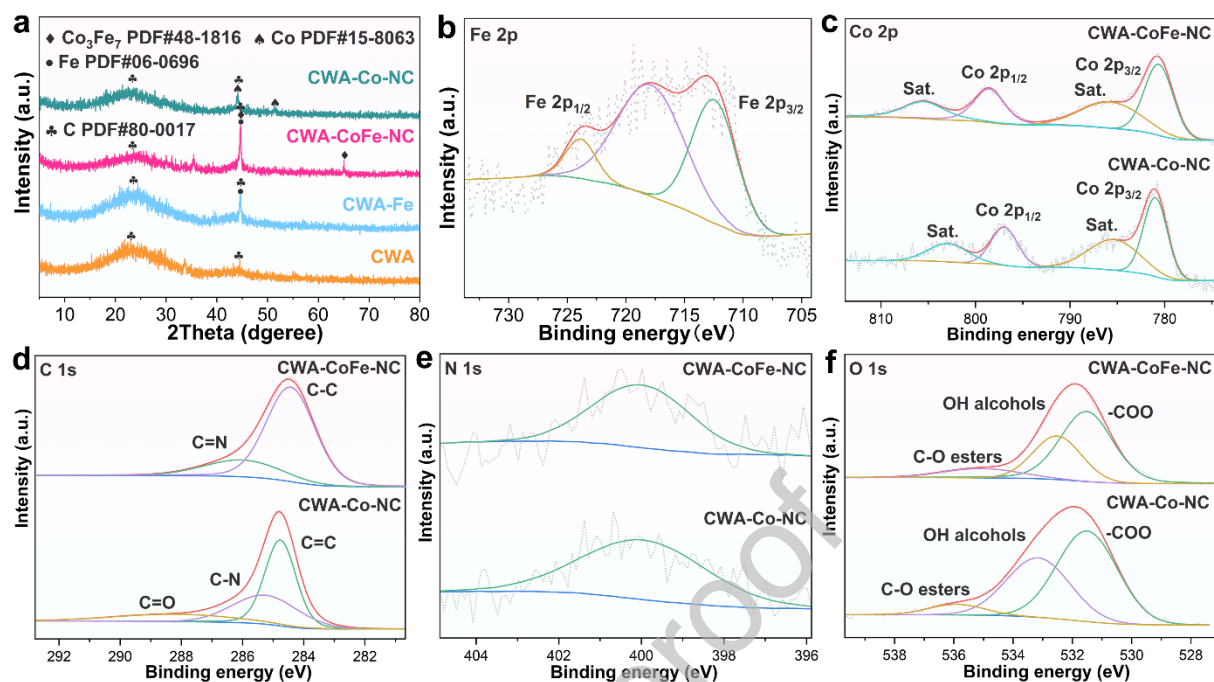COO, OH alcohols, and C-O esters, respectively [42,43].

Fig. 2. (a) XRD patterns of the samples. (b) XPS spectra of Fe 2p for CWA-CoFe-NC. XPS spectra of (c) Co 2p, (d) C 1s, (e) N 1s, and (f) O 1s for CWA-Co-NC and CWA-CoFe-NC.

The microstructures of the samples were observed by field-emission scanning electron microscopy (FE-SEM), as displayed in Fig. 3. It can be seen from the longitudinal (Figs. 3(a) and S3(a)) and cross-sectional directions (Figs. 3(b) and S3(b)) that CWA retains almost completely straight, oriented, and ordered pore channels. There are numerous fibers (~0.12 μm in thickness) loaded on the thin carbon wall in the longitudinal section, and a certain channel spacing of ~20 μm is maintained (Figs. 3(a) and S3(a)). The cross-section of porous CWA obtained after removing lignin and cellulose depicts regular parallel pore channels and the shape of the pore is a regular rectangle, similar to a rectangular honeycomb-like structure (Figs. 3(b) and S3(b)). The pore area is about 600 μm^2, and the carbon wall thickness is

13

around 2.5 μm. A large number of closed porous carbon walls can consume EMW to a great extent. After loading ZIF-67 and calcination, it can be seen from the longitudinal (Figs. 3(c) and S4(a)) and cross-sectional directions (Figs. 3(d) and S4(b)) of CWA-Co-NC that ZIF-67 derived nanoparticles are uniformly distributed on the pore wall of 3D porous pine carbon aerogel. The highly channelized 3D porous pine carbon aerogel is conducive to the uniform dispersion of nanoparticles to form uniform absorption sites. The pore wall of the pine carbon aerogel appears slightly folded in the cross-sectional direction. Furthermore, compared to CWA, CWA-Co-NC shows a slightly thinner pore wall. The EDS mapping image in Fig. S5 exhibits that the carbon aerogel is rich in heterogeneous N elements, and this kind of doping defect is favorable for dipole polarization, while the distribution of O elements is mainly derived from the rich oxygen-containing functional groups in the pine. Furthermore, the distribution of the Co element is mainly enriched in the ZIF-67 nanoparticle area. For CWA-Fe (Figs. 3(e, f) and S6), Fe-related species derived from Fe_3O_4 nanoparticles are also uniformly dispersed on the pore wall of the pine carbon aerogel. At the same time, CWA-Fe aerogel, like CWA-Co-NC aerogel, has some folds on the pore wall.

From the longitudinal (Figs. 3g and S7) and cross-sectional directions (Fig. 3(h)) of the CWA-CoFe-NC aerogel that the pore wall is thinner than that of CWA aerogel, but they also maintain an almost complete and wrinkle-free rectangular honeycomb-like pore structure. According to the EDS elemental mapping image (Figs. 3(i) and S8), C, N, and O elements are evenly dispersed on the carbon aerogel, while Co and Fe

14

elements are dispersed on the CoFe alloy nanoparticles. In addition, CoFe alloy nanoparticles generated by the reaction of ZIF-67 and Fe_3O_4 in pine carbon aerogel under high-temperature treatment are evenly dispersed on the pore wall of the aerogel. Importantly, these in-situ CoFe alloy nanoparticles are relatively loose in the carbon aerogel, which can save some raw material costs, which is different from the dense CoFe MOF-derived nanoparticles reported in previous work [44,45]. The parallel pore wall of carbon aerogel is similar to a "black box". When EMW enters the aerogel, the uniform and parallel pore structure of pine carbon aerogel promotes multiple scattering and reflection of EMW [37], which consumes the electromagnetic wave as much as possible.
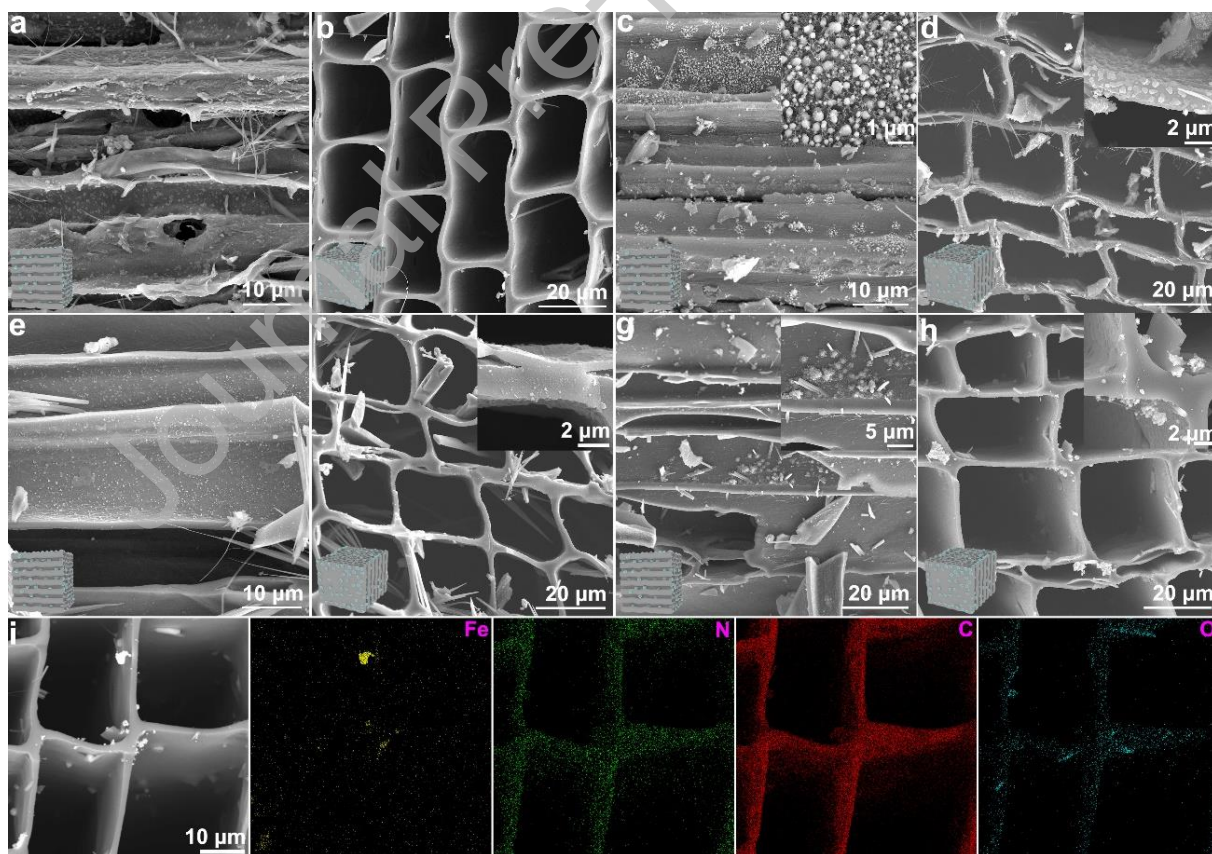

Fig. 3. SEM images of (a, b) CWA, (c, d) CWA-Co-NC, (e, f) CWA-Fe, and (g, h) CWA-CoFe-NC. (i) EDS element mapping image for CWA-CoFe-NC.

15

The microstructures of CWA-Co-NC and CWA-CoFe-NC were further analyzed by transmission electron microscopy (TEM). As shown in Figs. 4(a, d) and S9, the metallic Co nanoparticles with a diameter of ~25 nm were uniformly and highly distributed in CWA-Co-NC. Notably, the carbon aerogel is highly porous, including mesoporous and macropores, which greatly expands the consumption path of EMW. High-resolution TEM (HRTEM) image in Fig. 4(c) shows clear lattice fringes of 0.205 nm, which match well with the (111) plane of metallic Co [46]. On the other hand, CWA-CoFe-NC aerogel shows a similar porous carbon matrix with highly dispersed nanoparticles (Figs. 4(d, e) and S10). The diameter of these nanoparticles is only ~20 nm, which is limited by the porous structure of carbon aerogel, and further promotes the high dispersion of EMW absorption sites. The HRTEM images in Fig. 4(f) display highly ordered lattice fringes with a spacing of 0.21 nm, corresponding to the (110) plane of CoFe alloy [47], which is consistent with the above XRD data. Fig. 4(g) depicts that the aerogel is mainly composed of Co, Fe, N, O, and C elements. Co and Fe elements are located inside the nanoparticle, which also proves that CoFe alloy nanoparticles are embedded in the pore wall of carbon aerogel. Furthermore, the N element is evenly dispersed in the carbon matrix, indicating that aerogels are N-doped carbon, which agrees well with the above XPS results.
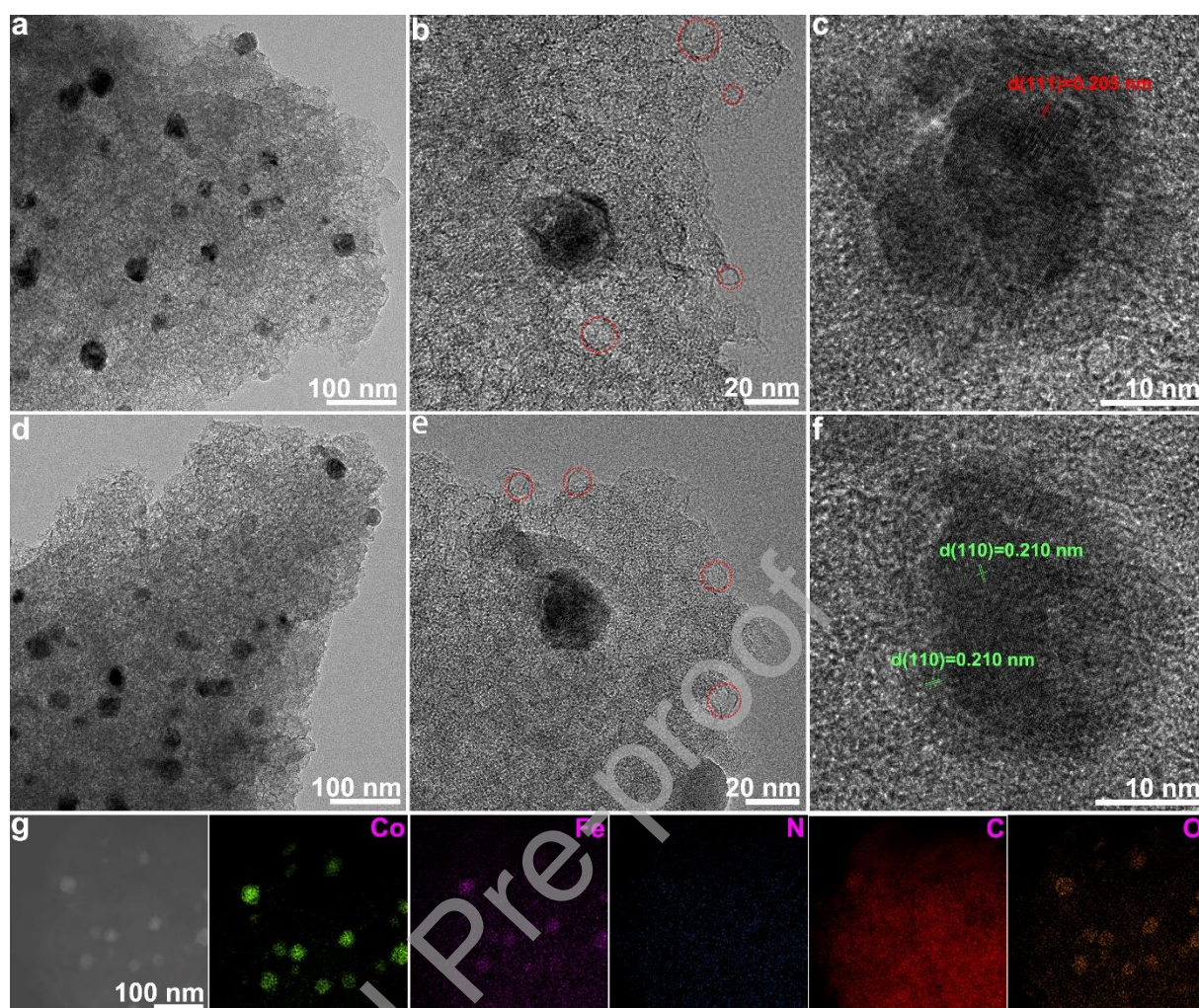
Fig. 4. (a,b,d,e) TEM and (c,f) HRTEM images of (a-c) CWA-Co-NC and (d-f) CWA-CoFe-NC. (g) EDS element mapping image for CWA-CoFe-NC.

With the highly dispersed small CoFe alloy nanoparticles, porous carbon aerogel with a rectangular honeycomb-like structure, and abundant N heteroatoms in the carbon matrix, it is expected that CWA-CoFe-NC inherits good EMW absorption performance. Fig. 5 depicts the 2D and 3D R_L curves of the samples. Due to the natural porous linear channel structure and the well-preserved pores of the pine carbon aerogel, the multiple scattering, reflection, and absorption can be maximum expanded during interaction with EMW, which promotes the pure CWA and enables a relatively good EMW absorption performance with an R_L value of -30.9 dB and an

17

EAB of 1.8 GHz at a matching thickness of 1.355 mm (Fig. 5(a) and (e)). After

loading ZIF-67 and calcination, the obtained CWA-Co-NC displays better EMW

absorption performance with an R_L value of -50.8 dB and an EAB of 2.08 GHz at a

matching thickness of 2.485 mm (Fig. 5(b)). 3D R_L curves show that CWA-Co-NC

has a more prominent EMW absorption capability in the low-frequency region and

has a wide effective frequency region (3.92-18 GHz) (Fig. 5(f)). Compared with CWA

aerogel, CWA-Fe aerogel reveals similar EMW absorption performance with an R_L

value of -46.1 dB and an EAB of 1.6 GHz at a matching thickness of 1.505 mm (Fig.

5(c)). From the 3D R_L curves, it can be seen that CWA-CoFe-NC shows more

prominent absorption capability in the high-frequency region (Fig. 5(g)). Notably,

after loading ZIF-67 and Fe_3O_4 simultaneously, the derived small CoFe alloy

nanoparticles exhibit a significant contribution to the WA-CoFe-NC, resulting in a

remarkable EMW absorption. Specifically, CWA-CoFe-NC shows an R_L value of -

61.6 dB and an EAB of 1.2 GHz at a matching thickness of 3.7 mm and a low

frequency of 4.92 GHz (Fig. 5(d) and (h)). Furthermore, for the high frequency of

16.64 GHz, CWA-CoFe-NC can also bring an R_L value of -58.2 dB and an EAB of

3.7 GHz at a matching thickness of only 1.2 mm, which combines the characteristics

of CWA and CWA-CoFe-NC. The excellent EMW absorption performance of CWA-

CoFe-NC is superior to a larger number of advanced EMW absorbers (Fig. 5(i) and

Table S1 in Supplementary Information). The temperature optimization experiment

reveals that the CWA-CoFe-NC calcined at 800 ℃ shows better EMW absorption

ability than the CWA-CoFe-NC calcined at 700 and 900 ℃ (Fig. S11), which can be

18

ascribed to the optimized size of alloy nanoparticle and the optimized graphitization
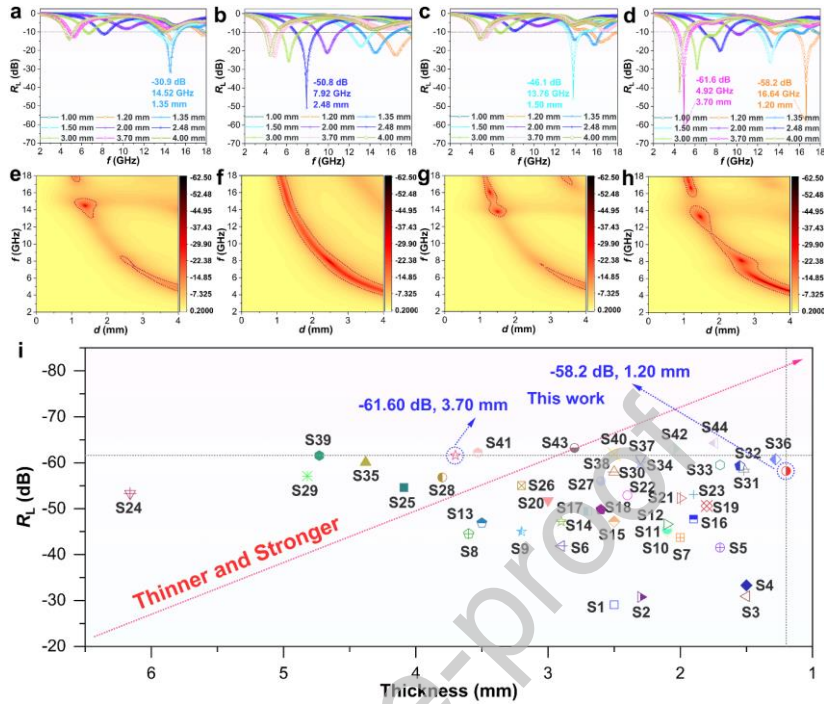
degree of the carbon aerogel.

Fig. 5. (a-d) 2D and (e-h) 3D R_L curves of (a, e) CWA, (b, f) CWA-Co-NC, (c, g) CWA-Fe, and (d, h) CWA-CoFe-NC. (i) Comparison of EMW absorption performance between CWA-CoFe-NC and other advanced EMW absorbers (see Table S1 for details).

To investigate the excellent EMW absorption performance of the porous CWA-CoFe-NC, the complex permittivity ($\varepsilon_r = \varepsilon'-j\varepsilon''$) and complex permeability ($\mu_r = \mu'-j\mu''$) were provided. As shown in Fig. 6(a-c), all the samples have high ε' (Fig. 6(a)), ε'' (Fig. 6(b)), and $\tan\delta_\varepsilon$ values (Fig. 6(c)), indicating that these aerogels have good energy storage and power consumption capabilities. Generally, ε'' is positively correlated with conductivity. The pine wood-derived carbon aerogel has a high conductivity. Therefore, CWA, CWA-Co-NC, CWA-Fe, and CWA-CoFe-NC have similar complex permittivity. The ε' and ε'' curves of these samples show a large

19

resonance peak in the high-frequency region (13-18 GHz). Besides, CWA-CoFe-NC also exhibits a large resonance peak in the low-frequency region (5-9 GHz), indicating its stronger polarization relaxation properties [48]. The multiple resonance peaks should originate from multiple polarizations, such as dipole polarization (N heteroatoms doping) and interface polarization (CoFe/NC, carbon aerogel/NC) in 3D porous CWA-CoFe-NC. On the other hand, these porous aerogels exhibit similar μ', μ'', and magnetic loss ($\tan\delta_\mu$) values in the low-frequency region (2-12 GHz) (Fig. 6(d-f)). The fluctuations in the μ' curves can be attributed to magnetic resonance in the absorber [49]. The μ'' curves display strong resonance peaks in the high-frequency region (12-18 GHz), indicating their exchange resonance properties [50]. These absorbers are dominated by dielectric losses in the low-frequency region, while in the high-frequency region, dielectric loss and magnetic loss work together. The effect of temperature on the ε', ε'', $\tan\delta_\varepsilon$, μ', μ'', and $\tan\delta_\mu$ values of CWA-CoFe-NC is shown in Fig. S12. It can be seen that the CWA-CoFe-NC calcined at 800 °C has a higher resonance peak in the low-frequency region (5-9 GHz) than the CWA-CoFe-NC calcined at 700 and 900 °C, indicating its better polarization relaxation characteristics. In addition, the resonance peaks (10-18 GHz) of CWA-CoFe-NC calcined at 800 °C are stronger than those of CWA-CoFe-NC calcined at 700 and 900 °C, confirming its better exchange resonance characteristics. As a result, the CWA-CoFe-NC calcined at 800 °C inherits a relatively better EMW absorption performance. Additionally, as shown in Fig. S12(c) and (f), the $\tan\delta_\varepsilon$ and $\tan\delta_\mu$ values of CWA-CoFe-NC calcined at 800 °C are larger than those of the samples calcined at 700 and 900 °C, indicating

better ability to dissipate EMW energy. These results further indicate that the CWA-

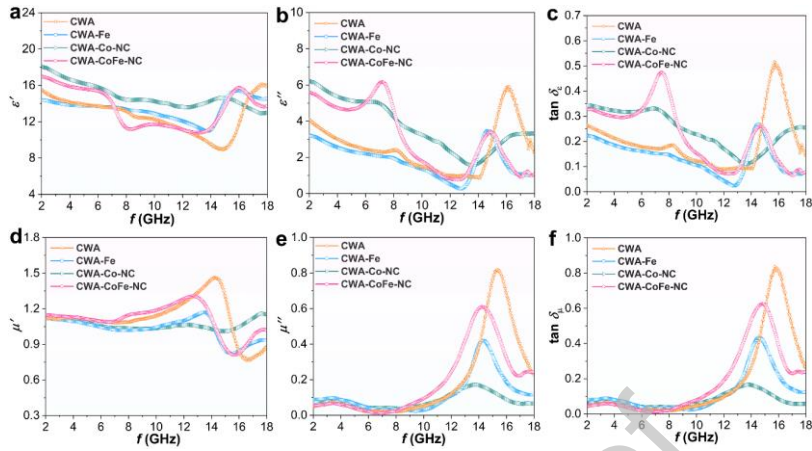CoFe-NC calcined at 800 °C exhibits better EMW absorption performance.

Fig. 6. (a) ε', (b) ε'', (c) tanδ_ε, (d) μ', (e) μ'', and (f) tanδ_μ curves of CWA, CWA-Co-NC, CWA-Fe, and CWA-CoFe-NC.

To further understand the polarization properties of the samples, the Debye theory

$((\varepsilon'-\varepsilon_\infty)^2 + (\varepsilon'')^2 = (\varepsilon_s-\varepsilon_\infty)^2)$ related to the relaxation phenomenon was introduced

[11,20]. With ε' and ε'' as the horizontal and vertical coordinates, respectively, the

resulting semicircle, the Cole-Cole semicircle, is the manifestation of the relaxation

phenomenon. The more Cole-Cole semicircles, the stronger the polarization

relaxation. As shown in Fig. 7(a), all the samples have Cole-Cole semicircles, which

prove the existence of the relaxation phenomenon. CWA and CWA-Co-NC consist of

a semicircle with a large radius and a slightly curved straight line, indicating their

similar polarization relaxation properties. In contrast, CWA-CoFe-NC has two Cole-

Cole semicircles with a large radius, indicating a strong relaxation phenomenon.

Furthermore, the CWA-CoFe-NC calcined at 700 and 900 °C show similar Cole-Cole

semicircles (Fig. S13).

The magnetic losses are mainly derived from the hysteresis, domain wall resonance

losses, exchange resonance, natural resonance, and eddy current losses [51]. Hysteresis and domain wall resonance losses can be neglected at frequency regions of 2-18 GHz [52]. If eddy current ($C_0 = \mu''(\mu')^{-2}f^1 = 2\pi\mu_0 d^2\sigma$) loss is the only mechanism of magnetic losses, the calculated C_0 with frequency is a constant value. As shown in Fig. 7(b), there is a significant variation in C_0 value in the frequency range of 2-6 GHz, indicating the presence of natural resonance behavior [53]. The C_0 values in the high-frequency region (14-18 GHz) are more variable, indicating that the magnetic loss is mainly contributed by natural resonance [54]. The C_0 values are almost unchanged in the frequency region of 6-12 GHz, indicating the presence of eddy current loss [55]. Therefore, these absorbers achieve natural resonance, exchange resonance, and eddy current loss. In the high-frequency region (14-18 GHz), the C_0 values of CWA-CoFe-NC calcined at 700 and 900 °C vary as much as that of CWA-CoFe-NC calcined at 800 °C (Fig. S14), indicating that the magnetic loss is mainly contributed by the natural resonance.

It is bealived that impedance matching ($Z = (\mu_r/\varepsilon_r)^{1/2}\tanh|j2\pi fd(\mu_r\varepsilon_r)^{1/2}/c|$) and electromagnetic attenuation ($\alpha = [((2)^{1/2}\pi f)/c]\times\{(\mu''\varepsilon'' - \mu'\varepsilon') + [(\mu''\varepsilon'' - \mu'\varepsilon')^2 + (\varepsilon'\mu'' + \varepsilon''\mu')^2]^{1/2}\}^{1/2}$) are the two main recognized mechanisms of EMW absorption [56]. As shown in Fig. 7(c), CWA has the highest α value, the largest attenuation constant, and the strongest attenuation ability in the whole frequency range. CWA-Co-NC has a lower α value and weak attenuation capacity. Moreover, CWA-CoFe-NC exhibits a distinct peak at ~7.5 GHz, which is not found in other samples and is further confirmed by Fig. S15. This should be attributed to the formation of CoFe alloy

22

nanoparticles promoting the attenuation of EMW. Additionally, CWA-CoFe-NC calcined at 800 °C shows the highest α value, indicating its best EMW absorption performance. On the other hand, the Z value should be greater than 0.3 and close to 1 to allow all EMW to easily pass through the air absorber interface without being reflected [57]. It can be found that the Z value of CWA-CoFe-NC is closest to 1, indicating that it enables the best impedance-matching characteristics and generates the best EMW absorption capacity. Importantly, CWA-CoFe-NC shows a Z value close to 1 at a matching thickness of 3.7 and 1.2 mm (Fig. S16), which is consistent with the excellent EMW absorption performance of CoFe/C@PC-800 at these two matching thicknesses. As expected, the Z value of CWA-CoFe-NC calcined at 800 °C is closest to 1 (Fig. S17).

Peak frequency vs. experimental matching thickness (d_m^{exp}) in a simulation of d_m (d_m^{sim}) vs. f_m curves around the $\lambda/4$ and $3\lambda/4$ curves is shown in Fig. 7(e) and (f). The relationship between d_m and f_m for CWA-CoFe-NC is determined to be consistent with the quarter-wavelength matching condition ($d_m = nc/(4f_m(|\mu_r||\varepsilon_r|)^{1/2}$, n = 1, 3, 5...). When the peak frequency (f_m) and matching thickness (d_m) satisfy this equation, the incident wave and reflected wave differ by 180 degrees, resulting in interference effects at the interface between the air and the absorber. Therefore, compared to CWA, CWA-Co-NC, and CWA-Fe, CWA-CoFe-NC exhibits the best EMW absorption performance, with high R_L values of -58.2 and -61.6 dB at matching thicknesses 1.2 and 3.7 mm, and EAB of 1.32 and 3.36 GHz, respectively. As shown in Fig. S18, in all samples, CWA-CoFe-NC calcined at 800 °C delivers higher

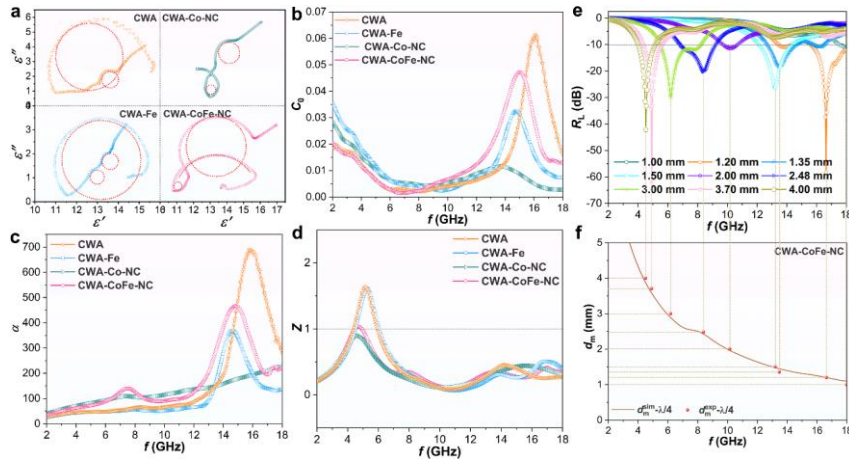reflection loss at lower matching thicknesses.

Fig. 7. (a) Cole-Cole plots of the samples. (b) C_0, (c) α, and (d) Z values of the samples. (e) 2D R_L values and (f) simulation of d_m (d_m^{sim}) vs. f_m curves of CWA-CoFe-NC.

Combining the above results and discussions, the EMW absorption mechanism of the 3D porous CWA-CoFe-NC aerogel can be proposed, as shown in Fig. 8. When EMW enters the absorber [58], the uniform linear channel structure of the pine carbon aerogel leads to multiple scattering, reflection, and absorption of EMW, which attenuates and dissipates EMW. Furthermore, the ZIF-67-derived graphitic carbon and the pine carbon aerogel build into a conductive network to enhance the conductive loss. At the same time, due to the multi-composition of the target products containing CoFe alloy nanoparticles, N-doped carbon, and carbon aerogel, a large number of interfaces are constructed, leading to good interface polarization [11,59]. In addition, the dipole polarization induced by the abundant N heteroatoms in the carbon matrix increases the EMW attenuation [20,60]. Finally, the formed CoFe alloy nanoparticles show high magnetic losses mainly derived from eddy current loss, natural resonance, and exchange resonance. As a result, the synergistic effect of good

dielectric loss, magnetic loss, and impedance matching promotes the EMW absorption performance [61,62].
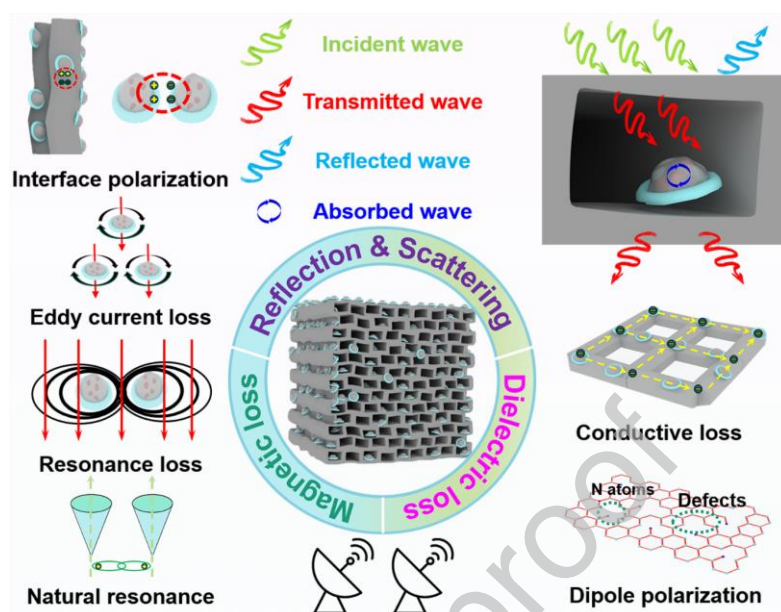

Fig. 8. EMW absorption mechanism of CWA-CoFe-NC.

In addition to the excellent EMW absorption properties, 3D porous CWA-CoFe-NC is expected to inherit good lightweight and mechanical properties. The macro images of CWA, CWA-Co-NC, CWA-Fe, and CWA-CoFe-NC aerogels (10 mm × 10 mm × 10 mm) standing on asparagus setaceous are shown in Fig. 9(a-d). It can be seen that the samples are well supported by the end of lightweight asparagus setaceous, without signs of downward bending, indicating the lightweight characteristics of the aerogels. The obtained aerogels present lightweight and adjustable shapes and sizes, which is because the structure of the pine has regular parallel channels in the cross-sectional direction and large cavities in the longitudinal direction. Furthermore, lignin and cellulose in the pine are removed during sample processing, which leads to the lightweight characteristics of the sample. As shown in Fig. 9(e-h), the mechanical properties of CWA-CoFe-NC aerogels were further investigated, and load-bearing

tests were conducted. In longitudinal and cross-sectional directions, a 3D porous CWA-CoFe-NC aerogel can easily support a 1 kg weight (Fig. 9(e) and (f)), while two 3D porous CWA-CoFe-NC aerogels can easily withstand a 2 kg weight (Fig. 9(g) and (h)). Moreover, the CWA-CoFe-NC aerogel displays no signs of compression and exhibits a certain degree of mechanical strength. The lightweight and certain mechanical properties of samples endow the EMW absorber with more application possibilities, especially in response to harsh environmental requirements. Generally, the heat treatment process improves the corrosion resistance of natural wood, but also decreases its mechanical properties, especially after the removal of lignin and cellulose. Interestingly, the mechanical properties of the constructed 3D porous CWA-CoFe-NC aerogel do not significantly decrease due to the regular parallel channels of pine, which are composed of extremely compact fibers that increase their toughness after heat treatment.
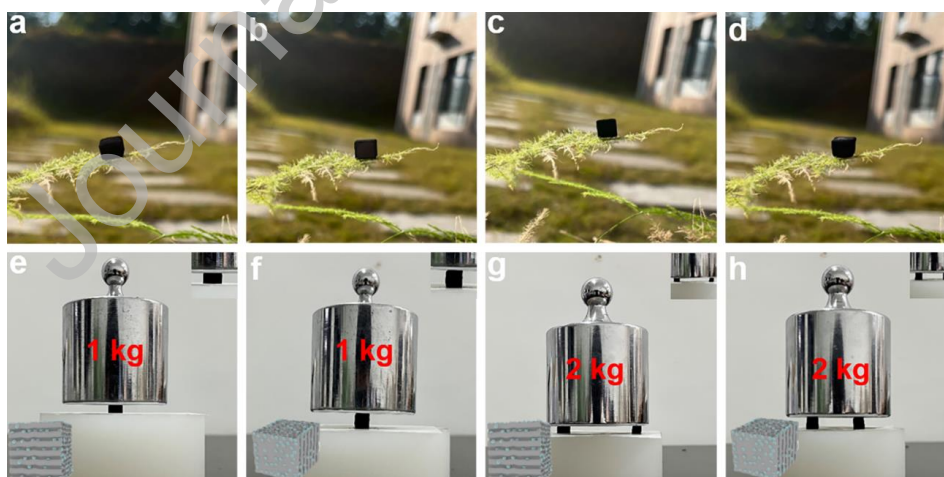

Fig. 9. Macro images of (a) CWA, (b) CWA-Co-NC, (c) CWA-Fe, and (d) CWA-CoFe-NC standing on asparagus setaceous. Macro images of (e, g) longitudinal and (f, h) cross-sectional directions for CWA-CoFe-NC supported by (e, f) 1 kg and (g, h)

2 kg weight. Insert image showing the enlarged macro image.

For extreme environments such as aerospace and aviation applications, EMW absorption materials also need to have good thermal stability and flame retardant properties [63]. Fig. 10 reveals the anisotropic flame retardant property of CWA-CoFe-NC. For carbonized pine obtained from the growth direction, the thermal energy mainly propagates through the straight and porous pore channels inside the pine. Therefore, the flame retardant performance of CWA-CoFe-NC varies in both the longitudinal and cross-sectional directions. When a petal is directly heated under an alcohol lamp, it can be observed that the petal is damaged after 10 s of heating (Fig. 10(a1-a5)), and the petal is completely damaged after 20 s. Importantly, when the petals are placed on carbonized pine in the longitudinal direction for heat treatment (Fig. 10(b1-b5)), the petals remain intact after 20 s but are damaged when heated to 35 s. In contrast, for carbonized pine in the cross-sectional direction, the petals are appropriately protected after 10 s (Fig. 10(c1-c5)), while the petals are damaged after heating for 30 s. Therefore, carbonized pine in both longitudinal and cross-sectional directions has better flame retardant performance, however, the thermal insulation performance is not as good as that of the axially carbonized pine due to the high thermal conductivity in the cross-sectional direction, its flame retardant property is not as good as that of aerogel longitudinal in the direction. Moreover, the CWA-CoFe-NC aerogel can maintain its original shape integrity after burning for 35 s on the alcohol lamp, which further indicates the excellent flame retardant property of the aerogel. These results suggest that anisotropic carbonized pine can be considered an

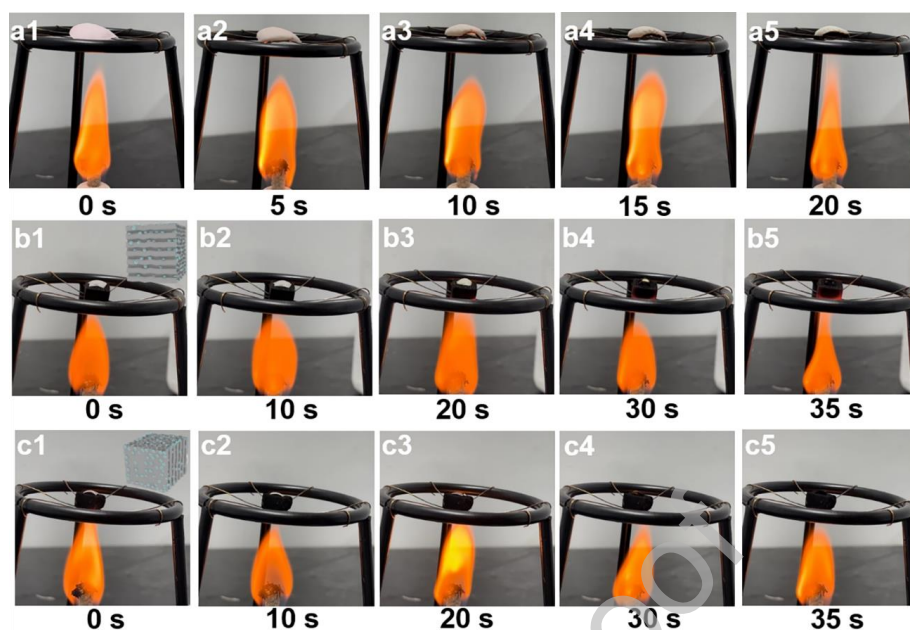intelligent insulation EMW absorption material.

Fig. 10. Photographs of flame retardant property of the CWA-CoFe-NC aerogel: (a1-a5) without aerogel, (b1-b5) longitudinal and (c1-c5) cross-sectional directions of CWA-CoFe-NC aerogel.

As mentioned above, good thermal stability is desired for the EMW absorption material in terms of thermal performance, thus exploring the thermal stability performance of CWA-CoFe-NC aerogel. Typically, aerogel is placed on an asbestos mesh, heated with an alcohol lamp, and naturally cooled, and the surface temperature is recorded. Furthermore, repeating the heating-cooling process to further observe the thermal stability of the aerogel. It can be seen that aerogel can be heated to about 380 °C in 30 s (Fig. 11(a)), and the heating rate is about 12 °C s^{-1}, indicating its good thermal conductivity. In addition, aerogel can be cooled to room temperature for 200 s (Fig. 11(b)), and the cooling rate is about 1.8 °C s^{-1}, which further indicates its good heat dissipation characteristics. This is because the 3D porous structure of pine promotes the aerogel to have faster heat conduction characteristics. The structural

stability of CWA-CoFe-NC aerogel is also evaluated by comparing the morphology before and after the thermal stability test. As displayed in the TEM images (Fig. S19(a) and (b)), the CoFe alloy nanoparticles uniformly dispersed in the porous carbon aerogel are well maintained after the thermal stability test. Furthermore, HRTEM images exhibit the lattice fringes of 0.21 nm (Fig. S19(c) and (d)), which can be attributed to the (110) plane of CoFe alloy, as described above. These results further confirm the merited stability features of CWA-CoFe-NC aerogel. To further evaluate the thermal stability of CWA-CoFe-NC aerogel, the aerogel was placed on the asbestos mesh, heated with an alcohol lamp and naturally cooled. The surface temperature of the aerogel and the appearance of the sample were recorded. Importantly, during the ten heating-cooling cycles, the surface temperature changes of the aerogel are highly consistent (Fig. 11(c)), indicating its good thermal management characteristics. In addition, the shape of the aerogel remains intact (Figs. 11(d) and S20), and the 3D porous structure is not damaged, which fully shows that the aerogel has excellent thermal stability.
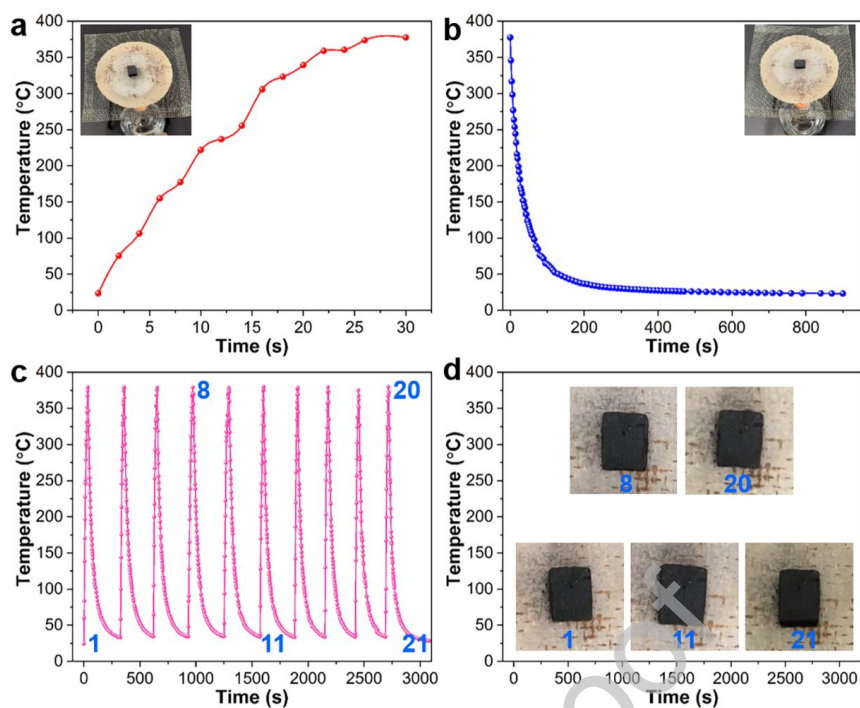
Fig. 11. Temperature evolution of CWA-CoFe-NC aerogel under alcohol lamp. (a) Temperature-rising curve and (b) temperature-cooling curve of aerogel surface. (c) Temperature evolution curves and (d) macro image of aerogel during heating-cooling cycles.

4. Conclusion

In summary, renewable pine woods with ordered pore channels in the longitudinal direction and rectangular pores in the cross-section direction are selected to load highly dispersed CoFe alloy nanoparticles formed by in-situ pyrolysis reaction between Fe_3O_4 nanospheres and ZIF-67 nanoparticles. The parallel pore wall of carbon aerogel is similar to a "black box", which consumes the electromagnetic wave as much as possible, while CoFe alloy nanoparticles are equivalent to the absorption site in the "black box". At the same time, with the highly dispersed small CoFe alloy nanoparticles, porous carbon aerogel with rectangular honeycomb-like structure, and

30

abundant N heteroatoms in the carbon matrix, the CWA-CoFe-NC aerogel inherits the excellent EMW absorption performance with R_L values of -61.6 and -58.2 dB at matching thicknesses of 3.7 and 1.2 mm, respectively. Benefiting from the reasonable design of the composite structure and composition, 3D porous aerogel also enables great potential for multifunctional applications. Specifically, good lightweight and mechanical properties are realized in the CWA-CoFe-NC aerogels due to their ordered pore channels and abundant rectangular pores. Furthermore, good flame retardant performance can ensure the serviceability of the target device in high/low-temperature environments. In addition, CWA-CoFe-NC aerogels show good thermal stability and thermal management characteristics. This work provides a novel and effective method for the preparation of lightweight, high-performance, and multifunctional EMW absorbers.

Supplementary Information

Supplementary Information is available in the online version of this article.

Acknowledgments

Data Availability statement

Data can be made available on request to the corresponding authors.

Author's contribution

All authors have made contributions to this work. Xiaojun Zeng planned, directed, and wrote the paper. Xiawen Peng performed the experiment. Ya Ning and Xiao Jiang performed the measurement. Xiaofeng Zhang provided concepts and design ideas. All authors read and approved the final manuscript.

Declaration of competing interest

The authors have no competing interests to declare that are relevant to the content of this article.

References

[1] M. He, H. Chen, H. Peng, Y.M. Zhou, Z.P. Song, Y.J. Wang, S.J. Feng, X.H. Bu, Chem. Eng. J. 456 (2023) 140985.

[2] X.J. Zeng, X. Jiang, Y. Ning, F.Y. Hu, B.B. Fan, J. Adv. Ceram. 12 (2023) 1562.

[3] C.H. Wei, L.Z. Shi, M.Q. Li, M.K. He, M.J. Li, X.R. Jing, P.B. Liu, J.W. Gu, J. Mater. Sci. Technol. 175 (2024) 194.

[4] C.B. Liang, H. Qiu, Y.L. Zhang, Y.Q. Liu, J.W. Gu, Sci. Bull. 68 (2023) 1195.

[5] X.J. Zeng, E.G. N. Li, G.H. Xia, N.H. Xie, Z.Y. Shen, M. Moskovits, R.H. Yu, J.

Eur. Ceram. Soc. 41 (2021) 7381.

[6] J.M. Yang, H. Wang, Y.L. Zhang, H.X. Zhang, J.W. Gu, Nano-Micro Lett. 16 (2024) 31.

[7] T.-B. Ma, H. Ma, K.-P. Ruan, X.-T. Shi, H. Qiu, S.-Y. Gao, J.-W. Gu, Chin. J. Polym. Sci. 40 (2022) 248.

[8] Y.Q. Guo, H. Qiu, K.P. Ruan, S.S. Wang, Y.L. Zhang, J.W. Gu, Compos. Sci. Technol. 219 (2022) 109253.

[9] X.J. Zeng, X.Y. Cheng, R.H. Yu, G.D. Stucky, Carbon 168 (2020) 606.

[10] J.R. Zhao, H. Wang, M.J. Chen, Y. Li, Z. Wang, C.Q. Fang, P.B. Liu, J. Colloid Interf. Sci. 639 (2023) 160.

[11] Z.Y. Jiang, Y.J. Gao, Z.H. Pan, M.M. Zhang, J.H. Guo, J.W. Zhang, C.H. Gong, J. Mater. Sci. Technol. 174 (2024) 195.

[12] X.J. Zeng, Y. Ning, H.H. Guo, N.H. Xie, R.H. Yu, Mater. Today Phys. 34 (2023) 101077.

[13] Y.X. Li, Y.J. Liao, L.Z. Ji, C.L. Hu, Z.H. Zhang, Z.Y. Zhang, R.Z. Zhao, H.W. Rong, G.W. Qin, X.F. Zhang, Small 18 (2022) 2107265.

[14] X.Y. Zhu, H.F. Qiu, P. Chen, G.Z. Chen, W.X. Min, Carbon 173 (2021) 1.

[15] Y. Wu, L. Chen, Y.X. Han, P.B. Liu, H.H. Xu, G.Z. Yu, Y.Y. Wang, T. Wen, W.B. Ju, J.W. Gu, Nano Res. 16 (2023) 7801.

[16] J.H. Luo, X.P. Li, W.X. Yan, P.C. Shu, J. Mei, Carbon 205 (2023) 552.

[17] X.J. Zeng, C. Zhao, X. Jiang, R.H. Yu, R.C. Che, Small (2023) 2303393.

[18] X.F. Zhou, Z.R. Jia, X.X. Zhang, B.B. Wang, W. Wu, X.H. Liu, B.H. Xu, G.L.

Wu, J. Mater. Sci. Technol. 87 (2021) 120.

[19] H.X. Zhang, Z.R. Jia, B.B. Wang, X.M. Wu, T. Sun, X.H. Liu, L. Bi, G.L. Wu, Chem. Eng. J. 421 (2021) 129960.

[20] J. Zhao, Z. Gu, Q. Zhang, Nano Res. (2023). https://doi.org/10.1007/s12274-023-6090-3.

[21] P. Xu, L.C. Meng, H.R. He, D.S. Qi, S. Wang, J.Y. Fang, X.G. Yue, Dalton Trans. 51 (2022) 17430.

[22] C. Li, X.S. Qi, X. Gong, Q. Peng, Y.L. Chen, R. Xie, W. Zhong, Nano Res. 15 (2022) 6761.

[23] J.M. Yang, Y.J Chen, X. Yan, X. Liao, H. Wang, C. Liu, H. Wu, Y. Zhou, H. Gao, Y.Y. Xia, H.X. Zhang, X. Li, T. Wang, Compos. Sci. Technol. 240 (2023) 110093.

[24] X.F. Zhou, Z.R. Jia, A.L. Feng, K.K. Wang, X.H. Liu, L. Chen, H.J. Cao, G. L. Wu, Compos. Commun. 21 (2020) 100404.

[25] L. Wang, X.T. Shi, J.L. Zhang, Y.L. Zhang, J.W. Gu, J. Mater. Sci. Technol. 52 (2020) 119.

[26] T.T. Bai, Y. Guo, D.D. Wang, H. Liu, G. Song, Y.M. Wang, Z.H. Guo, C.T. Liu, C.Y. Shen, J. Mater. Chem. A. 9 (2021) 5566.

[27] X. Qiu, L.X. Wang, H.L. Zhu, Y.K. Guan, Q.T. Zhang, Nanoscale 9 (2017) 7408.

[28] Z.J. Li, H. Lin, S.Y. Wu, X.Y. Su, T. Wang, W. Zhao, Y.J. Jiang, H.L. Ling, A.L. Meng, M. Zhang, Compos. Sci. Technol. 229 (2022) 109673.

[29] Y.P. Wei, Y.H. Yu, J.Z. Zhu, H.T. Song, Y.T. Wang, X.D. Wang, R.Z. Xiao, J.P.

Lin, J.W. Zhang, Y. Peng, J. Mater. Sci-Mater. Electron. 33 (2022) 24920.

[30] L. Huang, J.J. Li, Z.J. Wang, Y.B. Li, X.D. He, Y. Yuan, Carbon 143 (2019) 507.

[31] B. Zhao, P.W. Bai, S. Wang, H.Y. Ji, B.B. Fan, R. Zhang, R.C. Che, ACS Appl. Mater. Interfaces 13 (2021) 29101.

[32] M. Zhou, W.H. Gu, G.H. Wang, J. Zheng, C.C. Pei, F.Y. Fan, G.B. Ji, J. Mater. Chem. A 8 (2020) 24267.

[33] S.T. Gao, Y.C. Zhang, X.Z. Zhang, F.C. Jiao, T. Liu, H.X. Li, Y.H. Bai, C.L. Wu, J. Alloy. Compd. 952 (2023) 170016.

[34] X.T. Yang, J.H. Zhu, D. Yang, J.L. Zhang, Y.Q. Guo, X. Zhong, J. Kong, J.W. Gu, Compos. Pt. B-Eng. 185 (2020) 107784.

[35] X.J. Zeng, C. Zhao, Y.C. Yin, T.L. Nie, N.H. Xie, R.H. Yu, G.D. Stucky, Carbon 193 (2022) 26.

[36] S. Yin, Y. Huang, C. Deng, Y. Jiao, W.B. Wu, F. Seidi, H.N. Xiao, Compos. Sci. Technol. 218 (2022) 109184.

[37] Y. Xiong, L.L. Xu, C.X. Yang, Q.F. Sun, X.J. Xu, J. Mater. Chem. A 8 (2020) 18863.

[38] B. Wei, G.C. Xu, J.C. Hei, L. Zhang, T.T. Huang, Q. Wang, J. Colloid Interface Sci. 602 (2021) 619.

[39] G.Y. Chen, S. He, G.B. Shi, Y.S. Ma, C.C. Ruan, X. Jin, Q.L. Chen, X.Y. Liu, H.M. Dai, X.F. Chen, D.M. Huang, Chem. Eng. J. 423 (2021) 130184.

[40] T. Jin, H.X. Li, Y. Li, L.F. Jiao, J. Chen, Nano Energy 50 (2018) 462.

[41] F. Li, V.M. Basile, R.T. Pekarek, M.J. Rose, ACS Appl. Mater. Interfaces 6

(2014) 20557.

[42] J. Shin, J. Kwak, Y.G. Lee, S. Kim, C. Son, K.H. Cho, S.H. Lee, Y. Park, X.H. Ren, K. Chon, Environ. Res. 199 (2021) 111346.

[43] W. Zhang, C.Q. Huang, J.X. Zhu, Q.C. Zhou, R.H. Yu, Y.L. Wang, P.F. An, J. Zhang, M. Qiu, L. Zhou, L.Q. Mai, Z.G. Yi, Y. Yu, Angew. Chem. Int. Ed. 61 (2022) e202112116.

[44] Y.Q. Wang, H.G. Wang, J.H. Ye, L.Y. Shi, X. Feng, Chem. Eng. J. 383 (2020) 123096.

[45] Z.M. Song, X.F. Liu, X. Sun, Y. Li, X.Y. Nie, W.K. Tang, R.H. Yu, J.L. Shui, Carbon 151 (2019) 36.

[46] X.J. Zeng, Y.N. Tan, L. Xia, Q.Q. Zhang, G.D. Stucky, Chem. Commun. 59 (2023) 880.

[47] X.J. Ma, H. Chai, Y.L. Cao, J.Y. Xu, Y.C. Wang, H. Dong, D.Z. Jia, W.Y. Zhou, J. Colloid. Interface Sci. 514 (2018) 656.

[48] H.C. Luo, Y.Y. Lu, J. Qiu, ACS Appl. Mater. Interfaces 13 (2021) 32046.

[49] X.Y. Ren, Y.H. Song, Z.G. Gao, Y.L. Wu, Z.R. Jia, G.L. Wu, J. Mater. Sci. Technol. 134 (2023) 254.

[50] L. Liu, N. He, T. Wu, P.B. Hu, G.X. Tong, Chem. Eng. J. 355 (2019) 103.

[51] X.J. Zeng, T.L. Nie, C. Zhao, G.Z. Zhu, X.Z. Zhang, R.H. Yu, G.D. Stucky, R.C. Che, ACS Appl. Mater. Interfaces 14 (2022) 41235.

[52] R. Qiang, Y.C. Du, H.T. Zhao, Y. Wang, C.H. Tian, Z.G. Li, X.J. Han, P. Xu, J. Mater. Chem. A 3 (2015) 13426.

[53] F. Pan, X.F. Wu, D. Batalu, W. Lu, H.T. Guan, Adv. Powder Mater. 2 (2023) 100100.

[54] X.J. Zeng, G.M. Jiang, L.Y. Zhu, C.Y. Wang, M. Chen, R.H. Yu, ACS Appl. Nano Mater. 2 (2019) 5475.

[55] X.Q. Xu, F.T. Ran, Z.M. Fan, H. Lai, Z.J. Cheng, T. Lv, L. Shao, Y.Y. Liu, ACS Appl. Mater. Interfaces 11 (2019) 13564.

[56] J. Zhao, M. Li, X.G. Gao, J. Alloy. Compd. 915 (2022) 165439.

[57] L.L. Liang, W.H. Gu, Y. Wu, B.S. Zhang, G.H. Wang, Y. Yang, G.B. Ji, Adv. Mater. 34 (2022) 2106195.

[58] C.H. Zhou, C. Wu, M. Yan, Chem. Eng. J. 370 (2019) 988.

[59] Y. Zhou, X. Deng, H.N. Xing, H.Y. Zhao, Y.B. Liu, L.S. Guo, J. Feng, W. Feng, Y. Zong, X.H. Zhu, X.H. Li, Y. Peng, X.L. Zheng, Nano Res. 15 (2022) 6819.

[60] S.Y. Guo, Y.F. Bao, Y. Li, H.L. Guan, D.Y. Lei, T.J. Zhao, B.M. Zhong, Z.H. Li, J. Mater. Sci. Technol. 118 (2022) 218.

[61] F.Y. Hu, F. Zhang, X.H. Wang, Y.Y. Li, H.L. Wang, R. Zhang, H.X. Li, B.B. Fan, J. Adv. Ceram. 11 (2022) 1466-1478.

[62] K.J. Gong, Y.M. Peng, A. Liu, S.H. Qi, H. Qiu, Comps. Pt. A-Appl. Sci. Manuf. 176 (2024) 107857.

[63] W.H. Gu, S.J.H. Ong, Y.H. Shen, W.Y. Guo, Y.T. Fang, G.B. Ji, Z.C.J. Xu, Adv. Sci. 9 (2022) 220416.

Graphical abstract
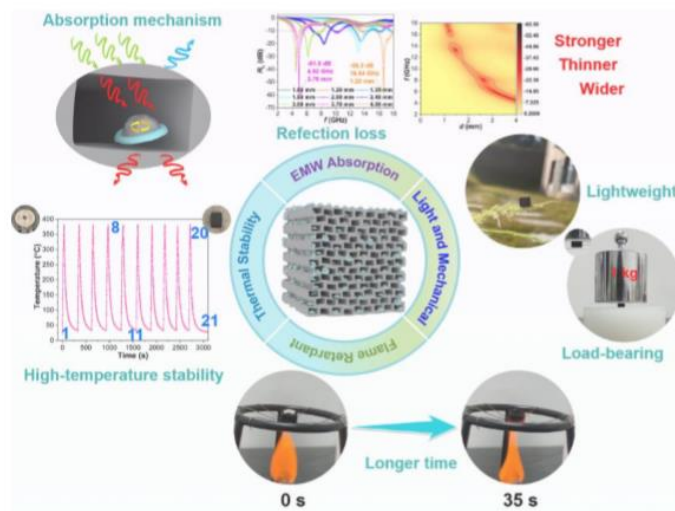
Declaration of interests

☒ The authors declare that they have no known competing financial interests or personal relationships that could have appeared to influence the work reported in this paper.

☐The authors declare the following financial interests/personal relationships which may be considered as potential competing interests: